THE JOURNAL OF PHYSICAL CHEMISTRY A
A JOURNAL OF THE AMERICAN CHEMICAL SOCIETY

pubs.acs.org/JPCA

Article

Free-Energy Landscape and Isomerization Rates of Au_4 Clusters at Finite Temperatures

Jiale Shi, Shanghui Huang, François Gygi, and Jonathan K. Whitmer*

Cite This: *J. Phys. Chem. A* 2022, 126, 3392−3400

Read Online

ACCESS | Metrics & More | Article Recommendations

ABSTRACT: In metallic nanoparticles, the geometry of atomic positions controls the particle's electronic band structure, polarizability, and catalytic properties. Analyzing the structural properties is a complex problem; the structure of an assembled cluster changes from moment to moment due to thermal fluctuations. Conventional structural analyses based on spectroscopy or diffraction cannot determine the instantaneous structure exactly and can merely provide an averaged structure. Molecular simulations offer an opportunity to examine the assembly and evolution of metallic clusters, as the preferred assemblies and conformations can easily be visualized and explored. Here, we utilize the adaptive biasing force algorithm applied to first-principles molecular dynamics to demonstrate the exploration of a relatively simple system, which permits a comprehensive study of the small metal cluster Au_4 in both neutral and charged configurations. Our simulation work offers a quantitative understanding of these clusters' dynamic structure, which is significant for single-site catalytic reactions on metal clusters and provides a starting point for a detailed quantitative understanding of more complex pure metal and alloy clusters' dynamic properties.

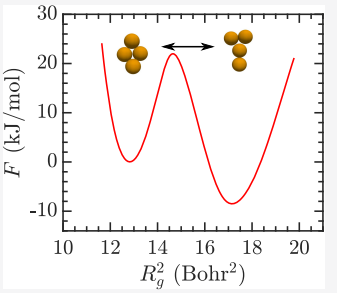

INTRODUCTION

In the assembly of nanoscopic and mesoscopic materials, clusters are important precursors where elemental units begin to aggregate.[1−4] The properties of initial aggregates that are formed control pathways available for subsequent assembly[5−7] and therefore the ultimate structure of the assembled materials. In the case of metallic nanoparticles, cluster geometry can impact the particle's electronic band structure, polarizability, and catalytic activity,[8−16] enabling many applications in gas sensing, pollution reduction, biology, nanotechnology, and catalysis.[17−26] Metal clusters' geometric packing properties[8] are very different from those of analogous clusters of isotropically attractive spheres.[3,4] This arises from the directional interactions imparted by electron orbitals, which are predominantly anisotropic in nature. For example, a four-particle colloidal cluster's stable structure is tetrahedral,[3] while the equivalent stable structures of metals have different structures governed by electron-sharing geometries;[27−29] Au_4 tends to adopt either a two-dimensional rhombus (◇) or a Y-shaped (Y) geometry.[28,30] As the number of atoms in a metal cluster increases, the structures become more intricate and have more isomers.[31]

Potential isomers of metal clusters may be identified by minimizing the energy in a DFT calculation without thermal fluctuations. Though these conformations can be long-lived, at finite temperature, a typical metallic cluster is dynamic[32] and exhibits rapid transitions between different structural isomers.[27,33−37] Experimental work on small clusters with spatiotemporal microscopic resolution by Imaoka et al.[27] has revealed that the metallic cluster Pt_4 randomly walks through several isomers and that the isomerization reactions follow simple first-order kinetics. Computational studies have utilized classical molecular dynamics simulation[29,38] and first-principles molecular dynamics simulation[31,39−42] to study the free-energy profiles of neutral gas-phase noble metal clusters and highlight the impact of temperature on the cluster stability. Most studies to date have focused on stable structures and ignored kinetic concerns that are known to be vital for practical applications.[43] Recent simulation work by Wang et al.[33] has, for example, demonstrated that Au_{20} rearranges dynamically to form single-atom catalytic active sites. Such behavior is essential to the function of nanoparticle-based heterogeneous catalysts. Understanding the kinetic behavior of clusters is thus key in determining the function of catalysts and engineering new materials.

When acting as catalysts, metallic clusters frequently exchange electrons with a substrate or ligand during the intermediate stages of a reaction.[44] Therefore, the charge of the cluster is often dynamically altered during a catalytic process and changes in different steps.[44] Computational studies at 0 K using DFT calculations, which have been compared to infrared spectroscopy on experiments, show that a charged cluster has a

Received: April 20, 2022
Published: May 18, 2022

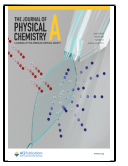

https://doi.org/10.1021/acs.jpca.2c02732
J. Phys. Chem. A 2022, 126, 3392−3400

different ground-state geometry than a neutral cluster.[9,14,45] Thus, it is significant to study how the charge affects the free-energy landscapes of metallic clusters at finite temperatures. Importantly, many of the properties of isomerization transitions, and how conformational states are influenced by the net charge on a metallic cluster, can be observed in small metallic clusters where they may be comprehensively understood.

Among all of the noble metals, gold clusters are the most widely explored.[30,31,46] Prior works have applied replica-exchange Monte Carlo and molecular dynamics[31,47] to study the free-energy landscape of neutral equilibrium gold clusters (Au_5–Au_{13}). These calculations require long equilibration times when the free-energy barriers are high between stable and metastable states.[48] Replica-exchange methods allow for an unbiased search of the potential energy substrates from which gold cluster structures can be identified. From results by Goldsmith et al.[31] on the free-energy landscape of Au_5, free-energy barriers are not well sampled, especially when the barrier is very high, causing rate calculations to be inaccurate. As the number of atoms in a gold cluster increases, the number of isomers increases significantly, resulting in more complex free-energy landscapes.[31] In this work, we choose Au_4 as a representative cluster and investigate the free-energy landscape of gas-phase neutral and charged Au_4 clusters to understand their thermodynamic and structural properties at different temperatures. The Au_4 cluster discussed previously is the smallest gold cluster that has multiple stable isomers, which are illustrated in Figure 1. First-principles molecular dynamics

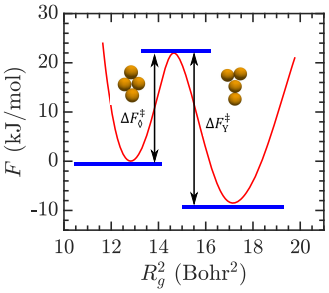

Figure 1. Free-energy landscape for Au_4 at 500 K, illustrating the relative height from each basin to the transition state ($\Delta F_i^\ddagger$). The rhombus ($\Diamond$) and Y-shaped (Y) configurations of the Au_4 cluster as observed in simulations are overlaid on the basins.

(FPMD) simulations coupled with advanced sampling methods[49] are applied to explore and analyze this system's stability and its isomerization rates. We additionally investigate the differences in the thermodynamic and structural properties between neutral and charged metal clusters to look into the mechanisms by which the charge would affect the metal clusters' stability at finite temperatures.

METHODS

The methods used in our calculation and information necessary to repeat or extend these calculations are discussed below.[1] Biased first-principles molecular dynamics simulations (FPMD) were carried out using the Qbox code[50] coupled with the SSAGES suite[51] in client–server mode.[43,49,52] Electronic structure computations necessary to obtain the forces on nuclei that are evolved in FPMD are carried out using density functional theory (DFT) with the PBE exchange–correlation functional. SG15-optimized norm-conserving Vanderbilt (ONCV) pseudopotentials[53] were used as implemented in the Qbox code.[50] A plane-wave basis set expanded to an energy cutoff of 45 Ry[2] represents the valence electrons, and the calculations include eight empty electronic states and Fermi smearing with an electronic temperature of 500 K. All calculations are performed without restricting spin. We do not explore the effects of spin polarization in these calculations, though during preliminary work, we compared the forces arising when considering spin polarization explicitly and found its influence to be negligible, similar to the results of Liu et al.[40] Relativistic effects are included for core electrons in the construction of ONCV potentials, but are not included in the description of valence orbitals which determine the bonding of gold atoms. Relativistic effects could lead to some quantitative changes in the transition temperature or reaction equilibrium of the two cluster isomers but are unlikely to lead to qualitatively different behavior since the transition between cluster isomers is mainly driven by entropy contributions.

All FPMD calculations involve a periodic cubic cell with an edge length of a = 13.92 Å, which is large enough that the Au_4 cluster does not interact with its own periodic images. A Bussi–Donadio–Parrinello (BDP) thermostat[54] is used to sample the canonical ensemble. As Au is a relatively heavy atom, the FPMD simulation time step is set to be 1.935 fs for a balance of accuracy and efficiency. For each time step, 10 self-consistent field calculations are performed, each involving five wave-function optimizations. Simulation settings for both charged and neutral clusters are identical, aside from modifying the overall net charge in Qbox to $q_{tot} \in \{-1,0,1\}$.

Elucidating isomerization transition rates requires efficient sampling of rare events since free-energy barriers must be crossed. Enhanced sampling calculations proceed by applying a bias to collective variables to speed up the exploration of the simulated systems. Collective variables (CVs), closely related to the concept of reaction coordinates, are a low-dimensional projection of the high-dimensional space of FPMD simulations, which can clearly distinguish reactants from products and quantify the dynamical progress along the pathway from reactants to products.[55] Generally, this defines a vector-valued function from the space of nuclear positions to the reduced CV space, $\boldsymbol{\xi}$: $\mathbb{R}^{3N} \rightarrow \mathbb{R}^d$, where N is the number of atoms and d is the desired reduced dimensionality. For delineating two basins, it is typically sufficient to define a single collective variable (though this can lead to dynamical bottlenecks if poorly chosen[56]). Here, we opt for a single CV, the squared radius of gyration of the cluster R_g^2, defined as

$$R_g^2 = \frac{1}{4}\sum_{i=1}^{4}(\mathbf{x}_i - \mathbf{x}_{CM})^2 \quad (1)$$

R_g^2 captures the compactness of the cluster and is thus sufficient to distinguish the two stable conformers. Here, $\mathbf{x}_i$ and $\mathbf{x}_{CM}$ refer to the position of each particle and the center of mass, respectively. This CV is able to distinguish the stable isomers of Au_4, as shown in Figure 1, and has been demonstrated to be a useful variable in past investigations for driving transitions between compact and extended clusters.[4] Values at each basin in Figure 1 are approximately $R_{g,\Diamond}^2 \approx 12.8$ (Bohr)^2 and $R_{g,Y}^2 \approx 17.2$ (Bohr)^2. These positions necessarily shift slightly when the temperature or charge state is modified.

Advanced sampling is carried out using the adaptive bias force (ABF) algorithm,[57] as implemented in SSAGES.[51] The

https://doi.org/10.1021/acs.jpca.2c02732
J. Phys. Chem. A 2022, 126, 3392–3400

ABF method is constructed to swiftly surmount large barriers in free energy by negating the forces that act to restore a configuration to a stable basin; as such, it is not only capable of accurately obtaining information about the relative free energies of basins but can also accurately sample the barriers between them, enabling the estimation of the transition rates using methods such as transition-state theory (TST). Other sampling techniques could potentially be used. Provided the CV used is a sufficiently good approximation of the true reaction coordinate, ABF can be used to swiftly scale and accurately determine free-energy barriers in reacting processes; this is, in particular, beneficial when using FPMD as the underlying algorithm to sample configurations.

We utilize four walkers[58] to accumulate the ABF bias on R_g^2, which is accumulated within the interval [11.5, 20.5] $(\text{Bohr})^2$ encompassing both basins of interest. When walkers wander outside this grid, a restoring force is applied outside of an initial unbiased buffer zone having a thickness of 0.3 $(\text{Bohr})^2$ to nudge the system back toward the region of interest. The one-dimensional region utilizes 90 bins, and the restoring forces are generated by a half-harmonic potential with a spring constant of 0.1 hartree/$(\text{Bohr})^4$, centered at the edges of the buffer zones. The ABF algorithm requires a minimum number n_{visit} of visits to each grid region before the full force is applied to avoid overemphasizing relatively rare states with large mean forces that can render a simulation unstable; here, we set n_{visit} = 100. Prior to applying the ABF algorithm, each walker is run for a short time (≈1700 FPMD steps) to obtain a locally equilibrated state. Enhanced sampling calculations are then performed for another 1×10^6 FPMD steps. We find that these settings are sufficient to explore this system's basins and transition state.

With the converged free-energy landscape, we are able to explore transition rates using transition-state theory (TST). Specifically, here, we are interested in the isomerization rate of the Au_4 cluster, but our discussion below is general to the computation of any reaction rate where the free-energy landscape is known along a single collective variable or reaction coordinate. TST requires only minimal details about the energy surface in the immediate vicinity of transition-state barrier, reactant, and product basins. The general expression for a reaction rate in TST is[55]

$$k_{\text{TST}} = \frac{k_B T}{h} V_0^{n-1} \exp(-\beta \Delta F^{\ddagger}) \tag{2}$$

where the volume per molecule V_0 corresponds to the reference concentration and to the volume in the translational partition functions, n corresponds to the reaction order, and $\Delta F^{\ddagger}$ is the activation free energy. Equation 2 describes that to calculate the reaction rates for the first-order reaction, one merely needs to know the free-energy barrier of the transition states relative to the reactant basins. The information about free-energy barriers is accessible using advanced sampling capable of driving successfully through these regions. These calculations are greatly facilitated using accurate free-energy landscapes obtained through advanced sampling methods. It should be noted that more complex, multivariate expressions for TST can be used if the reaction coordinate is not accurately captured using a single CV; these could prove useful for studying isomerization rates between molecules in more complex clusters.

RESULTS AND DISCUSSION

Figure 2 shows a collection of converged free-energy landscapes of neutral Au_4 clusters at different temperatures

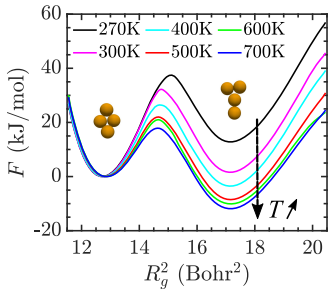

Figure 2. Free-energy landscapes of the Au_4 cluster with varying temperatures. At lower temperatures, the rhombus isomer is the dominant state; this transitions to the Y-shaped isomer at ≈400 K. The free-energy barriers also decrease with increasing temperature and are easily activated as they comprise only a few k_BT at high temperatures, meaning the two cluster forms will readily interconvert.

between 270 and 700 K. As can be reasonably hypothesized, the more compact, energetically favorable rhombus structure is favored at low temperatures, while the increased entropy within the Y-shaped structure is preferred as the temperature is increased. It is clear, however, that both configurations are at least metastable at all temperatures explored here. The wells for each are relatively deep, with the free-energy difference between the stable basin and transition state at approximately 20 kJ mol^{-1} or more for each temperature studied. At the lowest temperature, $\Delta F_{\Diamond}^{\ddagger} \approx 40$ kJ mol^{-1} and $\Delta F_{\text{Y}}^{\ddagger} \approx 25$ kJ mol^{-1}, corresponding to $\approx 18 k_BT$ and $\approx 11 k_BT$, respectively. This marks each configuration as extremely stable on short time scales typical of molecular simulations, with sampling of these transitions unlikely to be accessible without ABF or similar algorithms. The absolute depths of the free-energy wells remain in this order as the temperature increases, meaning that the activation barrier relative to k_BT is reduced significantly at higher temperatures; $\Delta F_{\Diamond}^{\ddagger}$ becomes ≈ 20 kJ mol^{-1} at 700 K ($\approx 3.5 k_BT$), so that transitions between the two basins become more dynamically favorable.

As temperature is increased, the relative stability of the rhombus decreases, with a concomitant increase in the stability of the Y-shaped cluster. At ≈400 K, the Y-shaped isomer becomes the dominant configuration due to its relatively higher entropy. Such effects have been previously noted to drive two-to-three dimensional transitions in Au_5−Au_{13} clusters[31] as temperature is increased. We can analyze the temperature dependence of cluster stability by computing the equilibrium constant for the isomerization reaction. To obtain this quantity, we subdivide the collective variable domain into two regions belonging to the rhombus or Y-shaped clusters. Note that the equilibrium probability of finding the system in one state is calculated by integrating all of the probabilities in that basin[55]

$$\tilde{P}(i) = \int_{\Xi_i} \mathrm{d}\xi \; \mathrm{e}^{-\beta F(\xi)} \tag{3}$$

where $\xi \in \Xi_i$ defines the CV of interest, and Ξ_i is the fraction of the domain corresponding to basin i. Note that this probability is unnormalized; one must divide out by the full partition function to obtain this quantity. Importantly, the

https://doi.org/10.1021/acs.jpca.2c02732
J. Phys. Chem. A 2022, 126, 3392−3400

probabilities phrased in this way define the occupancy rate for a system to be in one of the stable basins. We separate the free-energy landscape using the transition state and integrate each isomer's probability in the corresponding basin. Therefore, we obtain an expression for the occupancy rate of each isomer as

$$r_{\diamondsuit} = \frac{\tilde{P}_{\diamondsuit}}{\tilde{P}_{\diamondsuit} + \tilde{P}_{\mathrm{Y}}} \quad \text{and} \quad r_{\mathrm{Y}} = \frac{\tilde{P}_{\mathrm{Y}}}{\tilde{P}_{\diamondsuit} + \tilde{P}_{\mathrm{Y}}} \tag{4}$$

From Figure 3, the rhombus isomer is clearly dominant at low temperature. At 270 K, the occupancy rate of the rhombus

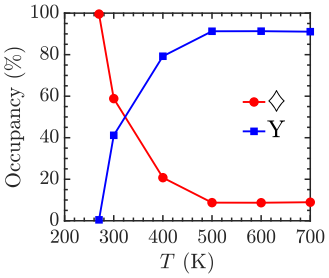

Figure 3. Occupancy rates (%) of ◇ (red circles) and Y (blue squares) isomers at different temperatures. At a low temperature (270 K), $r_{\diamondsuit} \approx 100\%$, while with increasing temperature, the occupancy rate of the Y isomer increases essentially monotonically. At the highest temperatures, the occupancy rates of the two states stabilize at approximate fractions: $r_{\diamondsuit} \approx 9$ % and $r_{\mathrm{Y}} \approx 91\%$.

isomer is almost 100%, while the occupancy rate of the Y-shaped isomer is almost zero. With increasing temperature, the occupancy rate of the rhombus isomer decreases, and the occupancy rate of the Y-shaped isomer increases. While the basins at 400 K are approximately equally deep (see Figure 2), there is a clear preference for the system to be in the Y basin due to its wider character and greater resulting probabilistic weight. Interpolating linearly on our measurements predicts that the isomers should be equally observed at approximately 330 K. As the temperatures increase to 500 K and beyond, the occupancy rates stabilize at approximate fractions $r_{\diamondsuit} \approx 9$ % and $r_{\mathrm{Y}} \approx 91$ %. As the temperature is increased further, the two basins would likely merge into a fluid-like single basin, while these would also compete with a dissociated gas-like state, though these transitions cannot be predicted from the data at hand.

The dynamic transition between two Au_4 isomers may be presented by a monomolecular reaction with first-order kinetics. Previous experimental results have shown that isomerization with one small metal cluster with no degenerate states obeys a first-order rate law.[27] Therefore, we calculate the reaction equilibrium constant K_{eq} following the first-order reaction rule

$$K_{\mathrm{eq}} = \frac{r_{\mathrm{Y}}}{r_{\diamondsuit}} \tag{5}$$

Here, we have replaced the typical concentrations in a rate constant expression with the relative populations of each species, which are equivalent in a system of Au_4 clusters, provided the system is not dense enough for clusters to interact. We plot the logarithm of the equilibrium constant ln K_{eq} as a function of temperature in Figure 4 (red circles). With increasing temperature, ln K_{eq} initially increases and eventually becomes approximately flat, mirroring the flattening of the

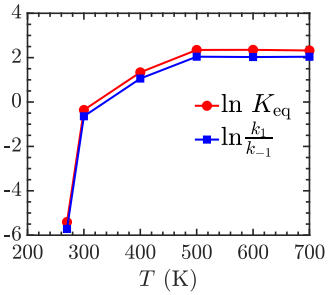

Figure 4. Equilibrium constant in log-scale ln K_{eq} (red circles) and ln $\frac{k_1}{k_{-1}}$ (blue squares) at different temperatures. These are numerically consistent, though ln $\frac{k_1}{k_{-1}}$ is slightly lower, owing to the different methods of accounting for entropy in the two calculations. See the text for more details.

ratios in Figure 3. Here, we also observe that the transition between clusters should occur at ≈300 K, where ln K_{eq} is zero.

Transition-state theory[55] may be used to calculate the transition rates at different temperatures. The dynamic transition between the metal cluster isomers is a first-order reaction;[27] thus, the expression of the reaction rate k is

$$k = \frac{k_{\mathrm{B}}T}{h} \exp(-\beta \Delta F^{\ddagger}) \tag{6}$$

Phrasing the reaction as

$$\diamondsuit \underset{k_{-1}}{\overset{k_1}{\leftrightarrow}} \mathrm{Y} \tag{7}$$

the forward and reverse rates are plotted in Figure 5. In general, with increasing temperature, both k_1 and k_{-1} increase,

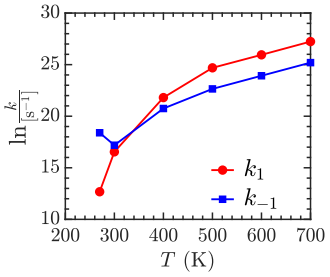

Figure 5. Forward transition (◇ → Y) reaction rate k_1 and the reverse transition (Y → ◇) reaction rate k_{-1} at different temperatures. In general, with increasing temperature, both k_1 and k_{-1} increase, as basins become less stable locally.

as is expected, since $\Delta F_i^{\ddagger}$ is relatively constant in magnitude over this temperature range, resulting in a decrease of $\Delta F_i^{\ddagger}/kT$. The exception is the reverse reaction k_{-1} at 270 K, which is significantly faster than the same reaction at 300 K due to the much lower free-energy barrier for the reverse reaction at 270 K. This type of feature would be expected for systems that are only marginally stable. Indeed, an increasing rate leads us to conjecture that the second stable basin may disappear in this CV at low enough temperatures. This perspective is supported by the occupancy statistics, which show the Y isomer to be essentially unpopulated at 270 K.

https://doi.org/10.1021/acs.jpca.2c02732
J. Phys. Chem. A 2022, 126, 3392−3400

To close these calculations, we note that we can compare the results of transition-state theory to our occupancy-based results for K_{eq} using the relationship

$$\ln K_{eq} = \ln \frac{k_1}{k_{-1}} \tag{8}$$

This quantity is plotted alongside our prior results in Figure 4. We note that the two are in broad agreement but that the equilibrium constant that we calculate from eq 8 is a bit smaller in comparison to that calculated from occupancy statistics. This is primarily due to the fact that K_{eq} from ABF takes into account the relative weight of the whole basin, which favors the increased entropy found in the Y-shaped isomer basin, though there could also be some small effects due to misalignment of the true reaction coordinate with R_g^2 that would cause $\Delta F_i^{\ddagger}$ to differ from the true activation energy. Since the differences are relatively small here, we can conclude that R_g^2 is a reasonable reaction coordinate for this transition.

To put these results within the context of typical ab initio simulations, we utilize the widely applied harmonic approximation method (HA)[59,60] to calculate the free-energy difference $\Delta F = F_{\diamondsuit} - F_{Y}$ to illustrate the differences that arise between the HA and more comprehensive sampling methods such as ABF. To apply the harmonic approximation, we first break down the partition function into contributions from translation t, rotation r, and vibration v along with an overall weight from the ground-state energy $U_{0,i}$ of a given conformation according to Peters[59] and Meng[3] and then apply harmonic well vibrational assumptions for the vibrational partition function

$$P_i \propto e^{-\beta F_i} = Z_i e^{-\beta U_{0,i}} = Z_{t,i} Z_{r,i} Z_{v,i} e^{-\beta U_{0,i}} \tag{9}$$

where i labels the conformation of interest, p_i is the probability in the canonical ensemble (NVT), Z_i is the partition function, F_i is the Helmholtz free energy, $Z_{t,i}$ is the translational partition function, $Z_{r,i}$ is the rotational partition function, and $Z_{v,i}$ is the vibrational partition function of conformation i. The translational components are essentially equal, but rotational, vibrational, and ground-state energies are necessarily different because of differences in the underlying symmetries, inertial axes, and potential energy landscapes of each conformation. For the rotational component,[61] we use the online ABC rotational constant calculator[62] to get the relative rotational constants A, B, C for $\diamondsuit$ and Y to plug into the relation

$$Z_r = \frac{\sqrt{\pi (kT)^3}}{\sigma \sqrt{ABC}} \tag{10}$$

The vibrational component is calculated using Qbox to find the vibrational modes of the cluster, using finite difference calculations of the dynamical matrix, keeping the six highest frequency modes.[3] We then use the quantum mechanical expression[59] for the vibrational free energy

$$F_v^{QM} = \beta^{-1} \sum_i \ln \left(\frac{1 - \exp(-\beta h \nu_i)}{\exp\left(-\frac{1}{2}\beta h \nu_i\right)} \right) \tag{11}$$

where the index i runs over the different vibrational modes of interest. Finally, adding in the ground-state energy difference computed using Qbox, $\Delta U_0 = U_{0,\diamondsuit} - U_{0,Y} \approx -1.2742$ kJ mol^{-1}, we arrive at the result plotted in Figure 6. Interestingly, while the ABF sampling shows a clear transition between the two clusters, the harmonic approximation uniformly favors the Y-shaped conformation, illustrating the key role played by entropy in these transitions and the importance of using full free-energy landscape sampling even in first-principles contexts.

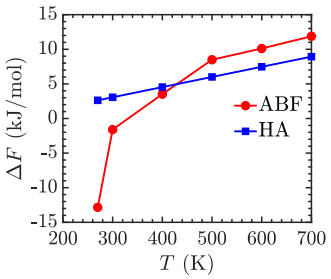

Figure 6. $\Delta F = F_{\diamondsuit} - F_{Y}$ at different temperatures calculated by the ABF sampling free-energy method (red dots) and harmonic approximation (HA) method (blue squares).

Charged Clusters. As noted, in real catalysts, metal clusters are not always neutral, and in many processes,[63] the charge distribution will change dynamically due to the ligands and substrate interactions involved in the catalytic cycle. As an example, Qiao et al.[64] found that in the Pt/FeO_x system, electrons transfer from a Pt atom to the FeO_x substrates, resulting in positively charged single Pt atoms Pt^+, which exhibits remarkable catalytic performance for CO oxidation and preferential oxidation. Similarly, Camellone et al.[44] have found that in the catalytic oxidation of CO using Au/CeO_2, the active gold atoms within the catalyst are positive ions. These species activate molecular CO and catalyze its oxidation. Interestingly, oxygen vacancies can attract the supported positively charged Au^+ and turn them into negatively charged Au^-. Since charge shifting plays a prominent role in catalytic processes, it is vital to investigate the effect of charge on the free energy of metal clusters. Here, we explore the influence that charge has on the conformational properties of Au_4 clusters in comparison to the neutral species.

We summarize our results in Figure 7. Some clear differences are manifest in the charged systems. We focus here on Au_4^+ and Au_4^-, as previous researchers only found at most one positive charge or one negative charge on a small Au

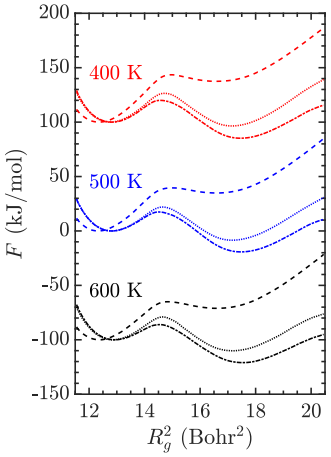

Figure 7. Free-energy landscapes of Au_4 (dotted line), Au_4^- (dash-dotted line), and Au_4^+ (dashed line) at 400 K (red), 500 K (blue), and 600 K (black).

https://doi.org/10.1021/acs.jpca.2c02732
J. Phys. Chem. A 2022, 126, 3392−3400

cluster for the catalysis process of Au clusters.[44,65−67] The first observed difference is the R_g^2 values of the two isomers. When neutral Au_4 loses one electron and becomes positively charged, the R_g^2 values of the two isomers become smaller than those of the neutral Au_4 cluster. This is somewhat surprising since one would expect charges centered at the nuclei to be more repulsive, thus expanding the cluster. However, this type of reasoning is inherently classical; the remaining electrons in the positive cluster create a cloud, which is effectively smaller than the neutral case, and these localized negative charges act to draw the nuclei closer together. This leads to the decrease of the R_g^2 values of the whole cluster. Interestingly, when neutral Au_4 gains one extra electron and becomes negatively charged, the R_g^2 values expand slightly, owing to the environment of the electron cloud pulling nuclei further apart. Notably, the effects are more pronounced for Au_4^+ than for Au_4^-. It is not clear how much these effects will generalize to larger clusters and higher valence, though it is likely the effects are more pronounced in the case of Au_4 than they would be in a larger cluster. Other factors, like the impact of electrostatic repulsion on the cluster size, must then also be considered.

The explanation may be bolstered by analyzing the HOMO (highest occupied molecular orbital) and LUMO (lowest unoccupied molecular orbital) of the Au_4 clusters.[68] For the rhombus isomer, the HOMO and LUMO have a similar antibonding "p-like" symmetry but are located on different pairs of atoms, as shown in Figure 8a,b. The HOMO orbital is

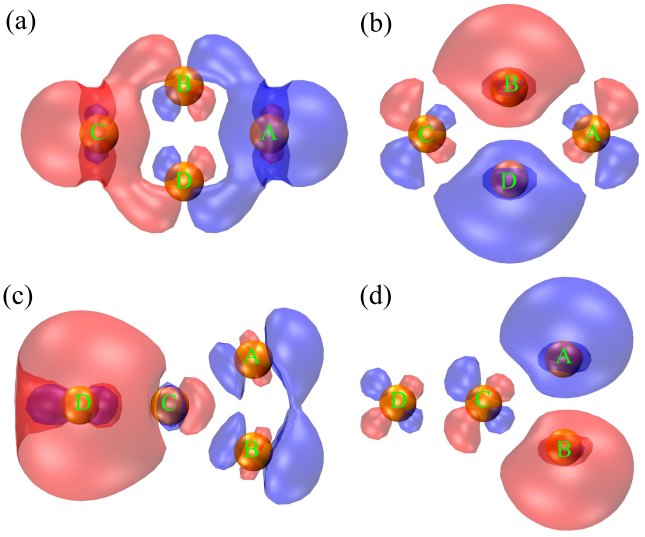

Figure 8. Molecular orbitals of Au_4 at the ground state (0 K). Rhombus isomer's HOMO (a) and LUMO (b). Y-shaped isomer's HOMO (c) and LUMO (d).

mostly localized on atoms A and C, whereas the LUMO is mostly localized on atoms B and D. Adding one extra electron to the LUMO increases the occupation of an antibonding state between B and D, which makes the bond length of B and D larger, resulting in an increased R_g^2. Removing one electron from the HOMO will reduce the occupation of an antibonding state between A and C, leading to a smaller bond between A and C resulting in a smaller R_g^2. The Y-shaped isomer's HOMO and LUMO are shown in Figure 8c,d. The HOMO orbital is mostly localized on A, B, and D, whereas the LUMO is mostly localized on A and B. Adding one extra electron to the LUMO increases the occupation of an antibonding state between A and B and makes the bond length of A and B larger resulting in a larger R_g^2.[68] Removing one electron from the HOMO will reduce the occupation of an antibonding state between A and D (or B and D) and make the bond length of A and D (or B and D) smaller resulting in a smaller R_g^2. This additionally breaks the symmetry of the Y-shaped isomer.

A pronounced effect is also observed in the relative free energy of the two isomers. Compared with the neutral Au_4 cluster, the relative free energy of the Y-shaped isomer in Au_4^+ increases significantly, and the Y-shaped isomer is metastable (and only weakly stable) at all studied temperatures; this is commensurate with our explanation relating cluster size to the electron cloud around the metal nuclei, which is unable to stretch as far when the cluster is positively charged.[45] Similarly, the effect of the negative charge is to favor less compact structures, destabilizing the rhombus isomers at all studied temperatures. The relative difference in depth can be quite significant, meaning a cluster that becomes charged when in a stable rhombus (or Y-shaped) configuration will experience a significant thermodynamic driving force toward the other conformation when gaining (or losing) an electron. Such effects could have a pronounced influence on the effectiveness of nanoparticles in heterogeneous catalysis, or on the relative structure of nanoparticles capped by specific ligands,[69−73] and signify an important avenue for subsequent research.

CONCLUSIONS

In this work, we investigate the thermodynamic and structural properties of Au_4 clusters (neutral, monoanionic, monocationic) in the gas phase by surveying the free-energy landscape and the isomerization rates. From this, a few general conclusions may be reached. One is that temperature is an important factor in determining the likely conformations, as it greatly affects the stability of Au_4 clusters with higher temperatures favoring larger entropy within the Y-shaped isomer. Exploring these free-energy landscapes, we are able to quantitatively calculate the equilibrium constant K_{eq} and transition rates k_1 and k_{-1} of the Au_4 isomerization reaction at different temperatures, observing an intriguing non-monotonicity, as one of the clusters becomes less mechanically stable at lower temperatures. Further, a cluster's charge significantly affects its preferred equilibrium energy in surprising ways, concomitantly affecting the relative free energy and stability of the two isomers. The dynamic charge distribution change in catalysis processes can impact the metal cluster's geometric structures. These observations are enabled by exploration of the full free-energy landscape available to the gold clusters using FPMD and the ABF method; accounting for thermalization and entropy using only density functional theory and the harmonic approximation would have led to different conclusions.

Many other essential factors in the behavior of metal clusters remain to be explored in relation to experimental observations that typically take place near an interface, such as the influence of substrate geometry[44] and the presence of defect points.[27] Apart from interconversion within one cluster's multiple isomers, catalysis processes have more complicated cluster-to-cluster transformations,[74] which make interesting targets for applications of these coupled FPMD and advanced sampling methods. Importantly, industrial catalysis widely uses alloy clusters,[75−77] and handling the thermodynamic and structural properties of complex alloys is thus essential and challenging. New advances in artificial intelligence and machine learn-

https://doi.org/10.1021/acs.jpca.2c02732
J. Phys. Chem. A 2022, 126, 3392−3400

ing[78,79] have offered new solutions to study the structural and transitional properties of complicated metal and alloy systems with faster computational speed while retaining accuracy and offer the potential to build on the framework established here to study complex physical processes in nanoparticles.

■ ASSOCIATED CONTENT

Accession Codes

Example scripts and information necessary to run the examples contained in this article are posted at https://github.com/shijiale0609/clustersFES. The Qbox code is available at http://qboxcode.org. SSAGES may be downloaded from http://ssagesproject.github.io.

■ AUTHOR INFORMATION

Corresponding Author

Jonathan K. Whitmer − *Department of Chemical and Biomolecular Engineering, University of Notre Dame, Notre Dame, Indiana 46556, United States;* orcid.org/0000-0003-0370-0873; Email: jwhitme1@nd.edu

Authors

Jiale Shi − *Department of Chemical and Biomolecular Engineering, University of Notre Dame, Notre Dame, Indiana 46556, United States*

Shanghui Huang − *Department of Chemistry and Biochemistry, University of Notre Dame, Notre Dame, Indiana 46556, United States*

François Gygi − *Department of Computer Science, University of California Davis, Davis, California 95616, United States;* orcid.org/0000-0002-2287-6017

Complete contact information is available at: https://pubs.acs.org/10.1021/acs.jpca.2c02732

Notes

The authors declare no competing financial interest.

■ ACKNOWLEDGMENTS

J.S., F.G., and J.K.W. acknowledge the support of MICCoM, the Midwest Center for Computational Materials, as part of the Computational Materials Sciences Program funded by the U.S. Department of Energy, Office of Science, Basic Energy Sciences, Materials Sciences and Engineering Division, for the development of algorithms and codes used within this work. Contributions of S.H. and J.K.W. were additionally supported by the U.S. National Science Foundation (Award No. DMR-1751988). J.S. and J.K.W. acknowledge the use of computational resources at the Notre Dame Center for Research Computing (CRC). J.S. and J.K.W. thank Dr. Elizabeth M. Y. Lee (U. Chicago) for assistance and discussions.

■ ADDITIONAL NOTES

[1]All required input files are available via GitHub at https://github.com/shijiale0609/clustersFES.

[2]While the choice of the energy cutoff has a nominal effect on ground-state calculations for these two configurations (which are within approximately 1 kJ mol^{-1} of each other), we have verified that this choice does not significantly affect the free-energy landscapes, which are dominated more by entropy and multiplicity of locally available states.

[3]All other modes are accounted for in the translational and rotational partition functions of the cluster. The six vibrational frequencies for ◇ are 35, 69, 86, 86, 143, and 162 cm^{-1} and the six vibrational frequencies for Y are 21, 37, 86, 94, 156, and 203 cm^{-1}.

■ REFERENCES

(1) Li, Z.-W.; Lu, Z.-Y.; Zhu, Y.-L.; Sun, Z.-Y.; An, L.-J. A simulation model for soft triblock Janus particles and their ordered packing. *RSC Adv.* **2013**, *3*, 813−822.

(2) Bianchi, E.; Panagiotopoulos, A. Z.; Nikoubashman, A. Self-assembly of Janus particles under shear. *Soft Matter* **2015**, *11*, 3767−3771.

(3) Meng, G.; Arkus, N.; Brenner, M. P.; Manoharan, V. N. The free-energy landscape of clusters of attractive hard spheres. *Science* **2010**, *327*, 560−563.

(4) Huang, S.; Quevillon, M. J.; Kyhl, S.; Whitmer, J. K. Surveying the free energy landscape of clusters of attractive colloidal spheres. *J. Chem. Phys.* **2020**, *152*, No. 134901.

(5) He, M.; Gales, J. P.; Ducrot, É.; Gong, Z.; Yi, G.-R.; Sacanna, S.; Pine, D. J. Colloidal diamond. *Nature* **2020**, *585*, 524−529.

(6) Wang, Y.; Jenkins, I. C.; McGinley, J. T.; Sinno, T.; Crocker, J. C. Colloidal crystals with diamond symmetry at optical lengthscales. *Nat. Commun.* **2017**, *8*, No. 14173.

(7) Chen, Q.; Whitmer, J. K.; Jiang, S.; Bae, S. C.; Luijten, E.; Granick, S. Supracolloidal reaction kinetics of Janus spheres. *Science* **2011**, *331*, 199−202.

(8) Zhai, H.-J.; Kiran, B.; Dai, B.; Li, J.; Wang, L.-S. Unique CO Chemisorption Properties of Gold Hexamer: Au6 (CO) n-(n= 0- 3). *J. Am. Chem. Soc.* **2005**, *127*, 12098−12106.

(9) Zhai, H.-J.; Pan, L.-L.; Dai, B.; Kiran, B.; Li, J.; Wang, L.-S. Chemisorption-induced structural changes and transition from chemisorption to physisorption in Au6 (CO) n-(n= 4- 9). *J. Phys. Chem. C* **2008**, *112*, 11920−11928.

(10) Liu, J.-X.; Filot, I. A.; Su, Y.; Zijlstra, B.; Hensen, E. J. Optimum particle size for gold-catalyzed CO oxidation. *J. Phys. Chem. C* **2018**, *122*, 8327−8340.

(11) Austin, N.; Johnson, J. K.; Mpourmpakis, G. Au13: CO adsorbs, nanoparticle responds. *J. Phys. Chem. C* **2015**, *119*, 18196−18202.

(12) Blaško, M.; Rajský, T.; Urban, M. A comparative DFT study of interactions of Au and small gold clusters Aun (n= 2-4) with CH3S and CH2 radicals. *Chem. Phys. Lett.* **2017**, *671*, 84−91.

(13) Chen, L.; Chen, B.; Zhou, C.; Wu, J.; Forrey, R. C.; Cheng, H. Influence of CO poisoning on hydrogen chemisorption onto a Pt6 cluster. *J. Phys. Chem. C* **2008**, *112*, 13937−13942.

(14) Lushchikova, O. V.; Huitema, D. M. M.; López-Tarifa, P.; Visscher, L.; Jamshidi, Z.; Bakker, J. M. Structures of Cun+ (n = 3−10) Clusters Obtained by Infrared Action Spectroscopy. *J. Phys. Chem. Lett.* **2019**, *10*, 2151−2155.

(15) Blaško, M.; Rajský, T.; Urban, M. A comparative DFT study of interactions of Au and small gold clusters Aun (n=2−4) with CH3S and CH2 radicals. *Chem. Phys. Lett.* **2017**, *671*, 84−91.

(16) Lang, S. M.; Bernhardt, T. M. Gas phase metal cluster model systems for heterogeneous catalysis. *Phys. Chem. Chem. Phys.* **2012**, *14*, 9255−9269.

(17) Häkkinen, H.; Abbet, S.; Sanchez, A.; Heiz, U.; Landman, U. Structural, Electronic, and Impurity-Doping Effects in Nanoscale Chemistry: Supported Gold Nanoclusters. *Angew. Chem., Int. Ed.* **2003**, *42*, 1297−1300.

(18) Mills, G.; Gordon, M. S.; Metiu, H. Oxygen adsorption on Au clusters and a rough Au(111) surface: The role of surface flatness, electron confinement, excess electrons, and band gap. *J. Chem. Phys.* **2003**, *118*, 4198−4205.

(19) Daniel, M.-C.; Astruc, D. Gold Nanoparticles: Assembly, Supramolecular Chemistry, Quantum-Size-Related Properties, and Applications toward Biology, Catalysis, and Nanotechnology. *Chem. Rev.* **2004**, *104*, 293−346.

(20) Yoon, B.; Häkkinen, H.; Landman, U.; Wörz, A. S.; Antonietti, J.-M.; Abbet, S.; Judai, K.; Heiz, U. Charging Effects on Bonding and

Catalyzed Oxidation of CO on Au8 Clusters on MgO. *Science* **2005**, *307*, 403−407.
(21) Pyykkö, P. Theoretical chemistry of gold. III. *Chem. Soc. Rev.* **2008**, *37*, 1967−1997.
(22) Häkkinen, H. Atomic and electronic structure of gold clusters: understanding flakes, cages and superatoms from simple concepts. *Chem. Soc. Rev.* **2008**, *37*, 1847−1859.
(23) Freund, H.-J.; Meijer, G.; Scheffler, M.; Schlögl, R.; Wolf, M. CO Oxidation as a Prototypical Reaction for Heterogeneous Processes. *Angew. Chem., Int. Ed.* **2011**, *50*, 10064−10094.
(24) Beret, E. C.; van Wijk, M. M.; Ghiringhelli, L. M. Reaction cycles and poisoning in catalysis by gold clusters: A thermodynamics approach. *Int. J. Quant. Chem.* **2014**, *114*, 57−65.
(25) Liu, J.-X.; Liu, Z.; Filot, I. A. W.; Su, Y.; Tranca, I.; Hensen, E. J. M. CO oxidation on Rh-doped hexadecagold clusters. *Catal. Sci. Technol.* **2017**, *7*, 75−83.
(26) Lang, S. M.; Bernhardt, T. M.; Chernyy, V.; Bakker, J. M.; Barnett, R. N.; Landman, U. Selective C-H Bond Cleavage in Methane by Small Gold Clusters. *Angew. Chem., Int. Ed.* **2017**, *56*, 13406−13410.
(27) Imaoka, T.; Toyonaga, T.; Morita, M.; Haruta, N.; Yamamoto, K. Isomerizations of a Pt4 cluster revealed by spatiotemporal microscopic analysis. *Chem. Commun.* **2019**, *55*, 4753−4756.
(28) Bonačić-Koutecký, V.; Burda, J.; Mitrić, R.; Ge, M.; Zampella, G.; Fantucci, P. Density functional study of structural and electronic properties of bimetallic silver−gold clusters: comparison with pure gold and silver clusters. *J. Chem. Phys.* **2002**, *117*, 3120−3131.
(29) Böyükata, M.; Belchior, J. C. Structural and energetic analysis of copper clusters: MD study of Cu n (n= 2-45). *J. Braz. Chem. Soc.* **2008**, *19*, 884−893.
(30) Gruene, P.; Butschke, B.; Lyon, J. T.; Rayner, D. M.; Fielicke, A. Far-IR Spectra of Small Neutral Gold Clusters in the Gas Phase. *Z. Phys. Chem.* **2014**, *228*, 337−350.
(31) Goldsmith, B. R.; Florian, J.; Liu, J.-X.; Gruene, P.; Lyon, J. T.; Rayner, D. M.; Fielicke, A.; Scheffler, M.; Ghiringhelli, L. M. Two-to-three dimensional transition in neutral gold clusters: The crucial role of van der Waals interactions and temperature. *Phys. Rev. Mater.* **2019**, *3*, No. 016002.
(32) Liu, J.-C.; Tang, Y.; Chang, C.-R.; Wang, Y.-G.; Li, J. Mechanistic insights into propene epoxidation with O2-H2O mixture on Au7/α-Al2O3: a hydroproxyl pathway from ab initio molecular dynamics simulations. *ACS Catal.* **2016**, *6*, 2525−2535.
(33) Wang, Y.-G.; Mei, D.; Glezakou, V.-A.; Li, J.; Rousseau, R. Dynamic formation of single-atom catalytic active sites on ceria-supported gold nanoparticles. *Nat. Commun.* **2015**, *6*, No. 6511.
(34) Xing, X.; Yoon, B.; Landman, U.; Parks, J. H. Structural evolution of Au nanoclusters: From planar to cage to tubular motifs. *Phys. Rev. B* **2006**, *74*, No. 165423.
(35) Bulusu, S.; Li, X.; Wang, L.-S.; Zeng, X. C. Evidence of hollow golden cages. *Proc. Natl. Acad. Sci. U.S.A.* **2006**, *103*, 8326−8330.
(36) Kryachko, E. S.; Remacle, F. The magic gold cluster Au20. *Int. J. Quant. Chem.* **2007**, *107*, 2922−2934.
(37) Olson, R. M.; Gordon, M. S. Isomers of Au8. *J. Chem. Phys.* **2007**, *126*, No. 214310.
(38) Arslan, H.; Güven, M. Dynamical and structural properties of Au 6 cluster. *ARI* **1998**, *51*, 145−148.
(39) Garzón, I. Z.; Kaplan, I.; Santamaria, R.; Vaisberg, B.; Novaro, O. Ab initio model potential and molecular dynamics simulation of Ag 6 clusters. *Z. Phys. D: At., Mol. Clusters* **1997**, *40*, 202−205.
(40) Liu, Z.; Yim, W.; Tse, J.; Hafner, J. Ab initio molecular dynamics study on Ag (n= 4, 5, 6). *Eur. Phys. J. D* **2000**, *10*, 105−114.
(41) Zhang, C.; Duan, H.; Lv, X.; Cao, B.; Abliz, A.; Wu, Z.; Long, M. Static and dynamical isomerization of Cu 38 cluster. *Sci. Rep.* **2019**, *9*, No. 7564.
(42) Bravo-Pérez, G.; Garzón, I.; Novaro, O. Non-additive effects in small gold clusters. *Chem. Phys. Lett.* **1999**, *313*, 655−664.
(43) Lee, E. M. Y.; Ludwig, T.; Yu, B.; Singh, A. R.; Gygi, F.; Nørskov, J. K.; de Pablo, J. J. Neural Network Sampling of the Free Energy Landscape for Nitrogen Dissociation on Ruthenium. *J. Phys. Chem. Lett.* **2021**, *12*, 2954−2962.
(44) Camellone, M. F.; Fabris, S. Reaction mechanisms for the CO oxidation on Au/CeO2 catalysts: Activity of substitutional Au3+/Au+ cations and deactivation of supported Au+ adatoms. *J. Am. Chem. Soc.* **2009**, *131*, 10473−10483.
(45) Ferrari, P.; Hou, G.-L.; Lushchikova, O. V.; Calvo, F.; Bakker, J. M.; Janssens, E. The structures of cationic gold clusters probed by far-infrared spectroscopy. *Phys. Chem. Chem. Phys.* **2020**, *22*, 11572−11577.
(46) Li, J.; Li, X.; Zhai, H.-J.; Wang, L.-S. Au20: A Tetrahedral Cluster. *Science* **2003**, *299*, 864−867.
(47) Beret, E. C.; Ghiringhelli, L. M.; Scheffler, M. Free gold clusters: beyond the static, monostructure description. *Faraday Discuss.* **2011**, *152*, 153−167.
(48) Machta, J. Strengths and weaknesses of parallel tempering. *Phys. Rev. E* **2009**, *80*, No. 056706.
(49) Sevgen, E.; Giberti, F.; Sidky, H.; Whitmer, J. K.; Galli, G.; Gygi, F.; de Pablo, J. Hierarchical coupling of first-principles molecular dynamics with advanced sampling methods. *J. Chem. Theory Comput.* **2018**, *14*, 2881−2888.
(50) Gygi, F. Architecture of Qbox: A scalable first-principles molecular dynamics code. *IBM J. Res. Dev.* **2008**, *52*, 137−144.
(51) Sidky, H.; Colón, Y. J.; Helfferich, J.; Sikora, B. J.; Bezik, C.; Chu, W.; Giberti, F.; Guo, A. Z.; Jiang, X.; Lequieu, J.; et al. SSAGES: Software Suite for Advanced General Ensemble Simulations. *J. Chem. Phys.* **2018**, *148*, No. 044104.
(52) Govoni, M.; Whitmer, J.; de Pablo, J.; Gygi, F.; Galli, G. Code interoperability extends the scope of quantum simulations. *npj Comput. Mater.* **2021**, *7*, No. 32.
(53) Schlipf, M.; Gygi, F. Optimization algorithm for the generation of ONCV pseudopotentials. *Comput. Phys. Commun.* **2015**, *196*, 36−44.
(54) Bussi, G.; Donadio, D.; Parrinello, M. Canonical sampling through velocity rescaling. *J. Chem. Phys.* **2007**, *126*, No. 014101.
(55) Peters, B. *Reaction Rate Theory and Rare Events*, Elsevier, 2017.
(56) Bussi, G.; Laio, A. Using metadynamics to explore complex free-energy landscapes. *Nat. Rev. Phys.* **2020**, *2*, 200−212.
(57) Darve, E.; Rodríguez-Gómez, D.; Pohorille, A. Adaptive biasing force method for scalar and vector free energy calculations. *J. Chem. Phys.* **2008**, *128*, No. 144120.
(58) Raiteri, P.; Laio, A.; Gervasio, F. L.; Micheletti, C.; Parrinello, M. Efficient reconstruction of complex free energy landscapes by multiple walkers metadynamics. *J. Phys. Chem. B* **2006**, *110*, 3533−3539.
(59) Peters, L. D. M.; Dietschreit, J. C. B.; Kussmann, J.; Ochsenfeld, C. Calculating free energies from the vibrational density of states function: Validation and critical assessment. *J. Chem. Phys.* **2019**, *150*, No. 194111.
(60) Sethna, J. *Statistical Mechanics: Entropy, Order Parameters, and Complexity*, Oxford University Press: USA, 2021; p. *14*.
(61) Cole, J. C.; Yao, J. W.; Shields, G. P.; Motherwell, W.; Allen, F. H.; Howard, J. A. Automatic detection of molecular symmetry in the Cambridge Structural Database. *Acta Crystallogr. B* **2001**, *57*, 88−94.
(62) Shattuck, T. W. ABC Rotational Constant Calculator. https://www.colby.edu/chemistry/PChem/scripts/ABC.html.
(63) Green, A. E.; Gentleman, A. S.; Schöllkopf, W.; Fielicke, A.; Mackenzie, S. R. Atomic Cluster Au_{10}^{+} Is a Strong Broadband Midinfrared Chromophore. *Phys. Rev. Lett.* **2021**, *127*, No. 033002.
(64) Qiao, B.; Wang, A.; Yang, X.; Allard, L. F.; Jiang, Z.; Cui, Y.; Liu, J.; Li, J.; Zhang, T. Single-atom catalysis of CO oxidation using Pt 1/FeO x. *Nat. Chem.* **2011**, *3*, 634−641.
(65) Khetrapal, N. S.; Wang, L.-S.; Zeng, X. C. Determination of CO Adsorption Sites on Gold Clusters Aun− (n = 21−25): A Size Region That Bridges the Pyramidal and Core−Shell Structures. *J. Phys. Chem. Lett.* **2018**, *9*, 5430−5439.
(66) Förstel, M.; Schewe, W.; Dopfer, O. Optical Spectroscopy of the Au4+ Cluster: The Resolved Vibronic Structure Indicates an Unexpected Isomer. *Angew. Chem.* **2019**, *131*, 3394−3398.

https://doi.org/10.1021/acs.jpca.2c02732
J. Phys. Chem. A 2022, 126, 3392−3400

(67) Jaeger, B. K. A.; Savoca, M.; Dopfer, O.; Truong, N. X. Photodissociation spectrum and structure of Au4+· H2O clusters. *Int. J. Mass Spectrom.* **2016**, *402*, 49−56.
(68) Liu, Z.; Qin, Z.; Xie, H.; Cong, R.; Wu, X.; Tang, Z. Structure of Au40/- 1 in the gas phase: A joint geometry relaxed ab initio calculations and vibrationally resolved photoelectron imaging investigation. *J. Chem. Phys.* **2013**, *139*, No. 094306.
(69) Scalise, E.; Srivastava, V.; Janke, E.; Talapin, D.; Galli, G.; Wippermann, S. Surface chemistry and buried interfaces in all-inorganic nanocrystalline solids. *Nat. Nanotechnol.* **2018**, *13*, 841−848.
(70) Chevrier, D. M.; Thanthirige, V. D.; Luo, Z.; Driscoll, S.; Cho, P.; MacDonald, M. A.; Yao, Q.; Guda, R.; Xie, J.; Johnson, E. R.; et al. Structure and formation of highly luminescent protein-stabilized gold clusters. *Chem. Sci.* **2018**, *9*, 2782−2790.
(71) Salorinne, K.; Man, R. W. Y.; Lummis, P. A.; Hazer, M. S. A.; Malola, S.; Yim, J. C.-H.; Veinot, A. J.; Zhou, W.; Häkkinen, H.; Nambo, M.; Crudden, C. M. Synthesis and properties of an Au6 cluster supported by a mixed N-heterocyclic carbene−thiolate ligand. *Chem. Commun.* **2020**, *56*, 6102−6105.
(72) Rusishvili, M.; Wippermann, S.; Talapin, D. V.; Galli, G. Stoichiometry of the Core Determines the Electronic Structure of Core−Shell III−V/II−VI Nanoparticles. *Chem. Mater.* **2020**, *32*, 9798−804.
(73) Jiang, T.; Qu, G.; Wang, J.; Ma, X.; Tian, H. Cucurbiturils brighten Au nanoclusters in water. *Chem. Sci.* **2020**, *11*, 3531−3537.
(74) Ren, X.; Fu, J.; Lin, X.; Fu, X.; Yan, J.; Wu, R.; Liu, C.; Huang, J. Cluster-to-cluster transformation among Au6, Au8 and Au11 nanoclusters. *Dalton Trans.* **2018**, *47*, 7487−7491.
(75) Li, Y.; Li, S.; Nagarajan, A. V.; Liu, Z.; Nevins, S.; Song, Y.; Mpourmpakis, G.; Jin, R. Hydrogen Evolution Electrocatalyst Design: Turning Inert Gold into Active Catalyst by Atomically Precise Nanochemistry. *J. Am. Chem. Soc.* **2021**, *143*, 11102−11108.
(76) León, I.; Ruipérez, F.; Ugalde, J. M.; Wang, L.-S. Probing the structures and bonding of auropolyynes, Au-(C≡C)n-Au-(n = 1−3), using high-resolution photoelectron imaging. *J. Chem. Phys.* **2018**, *149*, No. 144307.
(77) Jian, T.; Cheung, L. F.; Czekner, J.; Chen, T.-T.; Lopez, G. V.; Li, W.-L.; Wang, L.-S. Nb2©Au6: a molecular wheel with a short Nb-Nb triple bond coordinated by an Au6 ring and reinforced by σ aromaticity. *Chem. Sci.* **2017**, *8*, 7528−7536.
(78) Lamoureux, P. S.; Choksi, T. S.; Streibel, V.; Abild-Pedersen, F. Artificial Intelligence Real-time Prediction and Physical Interpretation of Atomic Binding Energies in Nano-scale Metal Clusters. 2020, arXiv2005.02572. arXiv.org e-Print archive. https://arxiv.org/abs/2005.02572.
(79) Deringer, V. L.; Bernstein, N.; Csányi, G.; Mahmoud, C. B.; Ceriotti, M.; Wilson, M.; Drabold, D. A.; Elliott, S. R. Origins of structural and electronic transitions in disordered silicon. *Nature* **2021**, *589*, 59−64.

https://doi.org/10.1021/acs.jpca.2c02732
J. Phys. Chem. A 2022, 126, 3392−3400